RESEARCH ARTICLE | JANUARY 08 2025

Open-boundary molecular dynamics of ultrasound using supramolecular water models

Special Collection: Molecular Dynamics, Methods and Applications 60 Years after Rahman

Maša Lah ; Nikolaos Ntarakas ; Tilen Potisk ; Petra Papež ; Matej Praprotnik

J. Chem. Phys. 162, 024103 (2025)
https://doi.org/10.1063/5.0238348

The Journal of Chemical Physics ARTICLE pubs.aip.org/aip/jcp

Open-boundary molecular dynamics of ultrasound using supramolecular water models

Cite as: J. Chem. Phys. 162, 024103 (2025); doi: 10.1063/5.0238348
Submitted: 11 September 2024 • Accepted: 23 December 2024 •
Published Online: 8 January 2025

Maša Lah,[1,2] Nikolaos Ntarakas,[1,2] Tilen Potisk,[1,2] Petra Papež,[1] and Matej Praprotnik[1,2,a)]

AFFILIATIONS

[1] Laboratory for Molecular Modeling, National Institute of Chemistry, Hajdrihova 19, SI-1001 Ljubljana, Slovenia
[2] Department of Physics, Faculty of Mathematics and Physics, University of Ljubljana, Jadranska 19, SI-1000 Ljubljana, Slovenia

Note: This paper is part of the JCP Special Topic on Molecular Dynamics, Methods and Applications 60 Years After Rahman.
[a)] **Author to whom correspondence should be addressed:** praprot@cmm.ki.si

ABSTRACT

Ultrasound can be used to manipulate protein function and activity, as well as for targeted drug delivery, making it a powerful diagnostic and therapeutic modality with wide applications in sonochemistry, nanotechnology, and engineering. However, a general particle-based approach to ultrasound modeling remains challenging due to the significant disparity between characteristic time scales governing ultrasound propagation. In this study, we use open-boundary molecular dynamics to simulate ultrasound waves in liquid water under ambient conditions by employing supramolecular water models, i.e., the Martini 3, dissipative particle dynamics, and many-body dissipative particle dynamics models. We demonstrate that our approach successfully reproduces the solution of the traveling wave equation and captures the velocity dispersion characteristic of high-frequency ultrasound waves.

I. INTRODUCTION

Ultrasound is a powerful and versatile tool in scientific research. Owing to its non-invasiveness, it has revolutionized medicine and materials science in the past century.[1] By leveraging acoustic waves with frequencies above 20 kHz, it enables precise control and visualization of particles and tissues. Moreover, ultrasound irradiation can increase the permeability of biological membranes,[2] disrupt amyloid fibrils,[3] and modulate protein activity.[4] Several groups have reported simulations of biomolecules subjected to shock waves or ultrasonic pressure fields of various frequencies and amplitudes.[5–12]

To accurately model ultrasound propagation in fluids, both compressibility and viscosity should be considered.[13,14] Compressibility, measuring a fluid's resistance to sustain volume changes under pressure, is crucial in determining the thermodynamic speed of sound c, as implied by $c = (\beta_S \rho_0)^{-1/2}$. Here, β_S is the adiabatic compressibility and ρ_0 is the equilibrium mass density. However, acoustic energy is dissipated in real fluids and sound waves are attenuated. The main source of attenuation can be attributed to viscous effects,[15] which ultimately determine the penetration depth of sound waves. In addition, the penetration depth is influenced by the frequency of the propagated sound wave and is known to decrease with increasing frequency. To illustrate, in water, MHz acoustic waves can penetrate several centimeters deep, while THz waves are absorbed on the nanometer scale.[1,13,14]

Sound waves are commonly simulated using continuum mesh-based methods, e.g., the boundary element method[16] and the finite element method.[17] It has been shown that hydrodynamics holds at surprisingly small scales,[18] which makes it possible to use the continuum theory even at the mesoscale. However, at these small scales, molecular discreteness becomes significant, as particles experience thermal motion that is negligible for macroscopic bodies, such as airplanes and submarines. To address this, fluctuating terms must be incorporated into hydrodynamic field theories, as pioneered by Landau and Lifshitz (LL).[19]

Alternatively, coarse-grained (CG) particle-based methods, such as the smoothed particle hydrodynamics (SPH)[20] and dissipative particle dynamics (DPD),[21–23] have shown significant potential for acoustic wave simulations.[5,24,25] In these approaches, the CG particles represent chunks of fluid that traverse the domain. This conceptually straightforward framework enables the exploration of

time and length scales that are typically inaccessible with conventional microscopic simulations. To overcome the limitations associated with the separation of characteristic scales governing ultrasound propagation, hybrid continuum-particle methods have been proposed.[26–31] An example is the molecular dynamics/fluctuating hydrodynamics (MD/LL-FH),[26] where a standing ultrasound wave is imposed by modifying the governing LL-FH equations for the cells at the beginning of the simulation domain, while the periodic boundaries of the system remain unchanged.

Studying the propagation and attenuation of sound waves requires careful implementation of boundary conditions. For instance, Asano *et al.*[32,33] used a sinusoidally oscillating wall to generate sound waves and applied a locally implemented Langevin thermostat near the opposing wall to dampen them. However, confined liquids are inherently affected by finite-size effects, which can significantly influence its behavior.[34,35] Similarly, Delgado-Buscalioni *et al.*[36] used a hybrid continuum-molecular dynamics (triple-scale) scheme and rigid walls in the outer continuum region to induce shear flow. In the triple-scale scheme, the boundary conditions are transmitted to the molecular dynamics (MD) domain via a flux exchange scheme, rendering the MD region an open system that exchanges mass, energy, and momentum with its surroundings.

Recently, it has been shown that the open-boundary molecular dynamics (OBMD) method,[37] which is used to simulate the particle domain of the triple-scale scheme mentioned above, enables one to simulate ultrasound waves in an open system using particles without changing Newton's equations of motion in the bulk.[24] OBMD is a combination of two (multiscale) MD methods, i.e., the adaptive resolution scheme (AdResS)[38,39] and open MD,[40,41] utilizing additional external forces to impose boundary conditions on the system. Sound waves are introduced as a time-dependent sinusoidal pressure perturbation.[28] Building on the work of Papež and Praprotnik,[24] where OBMD was used to study the propagation of ultrasound through liquid water described by the mesoscopic DPD[21,22] model, we employ the latter alongside additional supramolecular water models, i.e., the Martini 3[42] and the many-body DPD (MDPD)[43,44] models, in a new implementation of OBMD within Mirheo, a high throughput DPD simulation package.[45] This serves as a verification of the OBMD implementation in Mirheo. It allows us to study how the properties of selected water models and thermostat parameters influence their macroscopic properties, e.g., the shear viscosity, speed of sound, and attenuation coefficient. Finally, we explore how ultrasound attenuation and speed of sound vary with frequency.

II. THEORETICAL BACKGROUND AND METHODS

A. Attenuation and dispersion

Attenuation of sound waves has multiple sources that can be roughly divided into those related to fluids' intrinsic properties and those related to the boundaries of a medium.[14] Focusing on the former, the main contributions to sound absorption are due to the viscous effects that occur when expansion and compression accompany sound propagation, the transfer of thermal energy from high-temperature condensations to lower ones, and the structural relaxation associated with the volume changes during acoustic compression and its reversal.[13,14,46] Sound absorption can be phenomenologically attributed to a time lag between the pressure fluctuations in a sound wave and the associated density variation.[15] In general, at low frequencies, the relaxation effects are negligible because of the slow-varying pressure changes in the wave. Under these conditions, sound propagates with the low-frequency limit of the speed of sound, denoted by c. In contrast, at higher frequencies, the pressure changes too rapidly and the fluid cannot reach its relaxed state during oscillations. At such high frequencies, the propagation speed of the disturbance, denoted by v_p, varies with frequency.

To describe acoustic waves in viscous fluid, we first consider the Navier–Stokes equation,

$$\rho_m\left[\frac{\partial \mathbf{v}}{\partial t} + (\mathbf{v}\cdot\nabla)\mathbf{v}\right] = -\nabla p + \left(\frac{4}{3}\eta + \eta_B\right)\nabla(\nabla\cdot\mathbf{v}) - \eta\nabla\times\nabla\times\mathbf{v}, \tag{1}$$

where ρ_m is the mass density, $\mathbf{v}$ is the velocity, p is the pressure, and η and η_B are the shear and bulk viscosity, respectively.[13,19] The last term of Eq. (1) represents the dissipation of acoustic energy related to turbulence and vorticity, which are in linear acoustics usually confined to small regions near boundaries and are of lesser importance.[13] When omitting the last term and linearizing the left side of Eq. (1), the use of the linearized equation of continuity,

$$\nabla\cdot\mathbf{v} = -\frac{\partial s}{\partial t}, \tag{2}$$

and the adiabat $p = \rho_0 c^2 s$, where $s = (\rho_m - \rho_0)/\rho_0$ stands for condensation, give the lossy wave equation,

$$\left(1 + \tau_s\frac{\partial}{\partial t}\right)\nabla^2 p = \frac{1}{c^2}\frac{\partial^2 p}{\partial t^2}. \tag{3}$$

Here,

$$\tau_s = \left(\frac{4}{3}\eta + \eta_B\right)/\rho_0 c^2 \tag{4}$$

is the viscous relaxation time. For larger density amplitudes, nonlinear effects from the pressure equation of state introduce a term $\sim p\frac{\partial p}{\partial t}$ in the lossy wave equation Eq. (3), resulting in the Burgers' equation for the pressure amplitude.[47] For a monochromatic wave $\exp(i\omega t)$, where $\omega = 2\pi\nu$ is the angular frequency, we obtain the Helmholtz equation,

$$\nabla^2 p + k_c^2 p = 0, \tag{5}$$

where

$$k_c = k - i\alpha = (\omega/c)/\sqrt{1 + i\omega\tau_s} \tag{6}$$

is the complex wavenumber. The phase velocity v_p and the attenuation coefficient α are expressed as

$$v_p = \frac{\omega}{k} = c\sqrt{2}\left[\frac{1 + (\omega\tau_s)^2}{\sqrt{1 + (\omega\tau_s)^2} + 1}\right]^{1/2}, \tag{7}$$

$$\alpha = \frac{\omega}{c}\frac{1}{\sqrt{2}}\left[\frac{\sqrt{1 + (\omega\tau_s)^2} - 1}{1 + (\omega\tau_s)^2}\right]^{1/2}. \tag{8}$$

For a plane wave traveling in the positive x direction, the solution to Eq. (5) is

$$p = p_0 e^{i(\omega t - k_c x)} = p_0 e^{-\alpha x} e^{i(\omega t - k x)}. \tag{9}$$

As the relaxation time of viscous absorption, Eq. (4), is comparable with the time between successive collisions of a particle in a liquid, the wavelength of a sound wave at a frequency close to the relaxation frequency is similar to the mean free path of the molecules. In this regime, molecular effects become significant, violating the continuum assumption underlying the Navier–Stokes equations. For this reason, the theory is only valid in the limit of small frequencies, i.e., when $\omega\tau_s \ll 1$.[13] In this limit, Eqs. (7) and (8) yield the following simpler forms:

$$\alpha \approx \frac{\omega^2}{2\rho_0 c^3}\left(\frac{4}{3}\eta + \eta_B\right) \tag{10}$$

and

$$v_p \approx c\left[1 + \frac{3}{8}(\omega\tau_s)^2\right]. \tag{11}$$

The presented theory predicts a quadratic dependence of the attenuation coefficient on frequency. Furthermore, it explains that the dispersion of sound propagation is $O(\omega\tau_s)^2$, which is small at low frequencies, but significant in the high-frequency regime.[13]

B. (Many-body) dissipative particle dynamics

To extract the details of the interaction of sound waves with water, we first resort to the mesoscopic DPD model, which is often used to simulate complex systems, such as blood,[48] polymers,[49] colloids,[50] and droplet dynamics.[51] In addition, it conserves the overall linear momentum and recovers the Navier–Stokes equations in the continuum limit,[22] which is crucial for our applications. The equations of motion for a DPD particle of mass m_i are

$$m_i \frac{\mathrm{d}\mathbf{v}_i}{\mathrm{d}t} = \sum_{j\neq i}\left(\mathbf{F}_{ij}^C + \mathbf{F}_{ij}^R + \mathbf{F}_{ij}^D\right), \qquad \frac{\mathrm{d}\mathbf{r}_i}{\mathrm{d}t} = \mathbf{v}_i, \tag{12}$$

where $\mathbf{F}_{ij}^C$, $\mathbf{F}_{ij}^R$, and $\mathbf{F}_{ij}^D$ are the conservative, random, and dissipative forces acting between particle i and j, respectively, and are defined as

$$\mathbf{F}_{ij}^C = a w(r_{ij})\hat{\mathbf{e}}_{ij}, \tag{13}$$

$$\mathbf{F}_{ij}^R = \sigma w_R(r_{ij})\Theta_{ij}\hat{\mathbf{e}}_{ij}, \tag{14}$$

$$\mathbf{F}_{ij}^D = -\gamma w_D(r_{ij})(\mathbf{v}_{ij}\cdot\hat{\mathbf{e}}_{ij})\hat{\mathbf{e}}_{ij}. \tag{15}$$

In DPD, the conservative force is a linear repulsive force of strength a, the random force accounts for the thermal fluctuations of the particles, while the dissipative force represents viscous damping and depends on the relative velocity of the particle pair. Here, $\mathbf{v}_{ij} = \mathbf{v}_i - \mathbf{v}_j$ and $\mathbf{r}_{ij} = \mathbf{r}_i - \mathbf{r}_j$ are the relative velocity and displacement of the particles, respectively, $\hat{\mathbf{e}}_{ij} = \mathbf{r}_{ij}/r_{ij}$, and $r_{ij} = |\mathbf{r}_{ij}|$. Furthermore, σ and γ are the controlling parameters of the random and dissipative forces, respectively, and Θ_{ij} is a Gaussian white noise variable, symmetric in particle indices ($\Theta_{ij} = \Theta_{ji}$) with zero mean and unit variance. $w(r)$, $w_R(r)$, and $w_D(r)$ are the conservative, random, and dissipative weight functions, respectively. Together, the random and dissipative forces act as a thermostat, maintaining the system's temperature T, which is set by the fluctuation–dissipation theorem given by

$$\sigma^2 = 2\gamma k_B T, \tag{16}$$

where k_B is the Boltzmann constant. The weight functions are defined as

$$w_D(r) = [w_R(r)]^2 = [w(r)]^{2s}, \tag{17}$$

where the exponent s is usually chosen in the region $0 \le s \le 1$, with higher values of s reducing the friction between particles, and

$$w(r) = \begin{cases} 1 - r/r_c, & r < r_c, \\ 0, & r \ge r_c. \end{cases}$$

Here, r_c is the cutoff radius.

Complex fluid behavior, such as phase separation and surface tension effects, are challenging to model with the standard DPD. On the other hand, these properties can be captured by using the MDPD model,[43,44] which is an extension of the DPD model that introduces a density-dependent repulsive term in the conservative force. The latter is defined as

$$\mathbf{F}_{ij}^C = a w(r_{ij})\hat{\mathbf{e}}_{ij} + b(\bar{\rho}_i + \bar{\rho}_j) w_d(r_{ij})\hat{\mathbf{e}}_{ij}, \tag{18}$$

where a and b are the interaction parameters, $w_d(r)$ is a weight function with a cutoff $r_d < r_c$,

$$w_d(r) = \begin{cases} 1 - r/r_d & r < r_d, \\ 0, & r \ge r_d, \end{cases}$$

and $\bar{\rho}_i$ is the local density of particle i, calculated as

$$\bar{\rho}_i = \sum_{i\neq j} \frac{15}{2\pi r_d^3} w_d^2(r_{ij}). \tag{19}$$

The equation of state (EOS) of MDPD for $r_c = 1$ is[52]

$$p = \rho k_B T + a\tilde{\alpha}\rho^2 + 2\tilde{\alpha}b r_d^4(\rho^3 - \tilde{c}\rho^2 + d\rho) - \frac{\tilde{\alpha}b r_d^4}{|a|^{1/2}}\rho^2, \tag{20}$$

where $\tilde{\alpha} = 0.101$, $\tilde{c} = 4.69$, and $d = 7.55$. If $b = 0$, MDPD reduces to standard DPD.

C. Open-boundary molecular dynamics (OBMD)

To simulate complex non-equilibrium conditions, we employ OBMD. In OBMD, the simulation box is divided into three regions, i.e., two buffer regions on the sides of the simulation box enclosing the central region of interest (ROI). The governing equations of motion, e.g., Eqs. (12)–(15) for DPD, remain unchanged in the ROI. The box is opened in one spatial direction, usually along the x axis, while in the remaining two (y and z directions), periodic boundaries are applied, as shown in Fig. 1. The buffers act as reservoirs for particles that are free to diffuse between the regions and

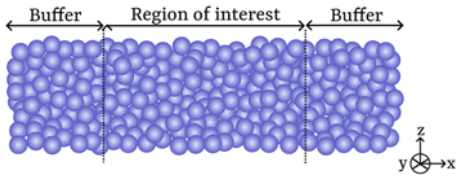

FIG. 1. Schematic of the OBMD scheme, where the simulation box is open along the *x* axis, and the ROI is enclosed by two buffers.

are deleted from the system when they diffuse across the outer border of the simulation box. To keep the number of particles in the buffers approximately constant, a simple feedback loop is utilized. The algorithm keeps track of $\Delta N = \Delta t/\tau_B(N_0 - N)$, where Δt is the time step, τ_B is the buffer relaxation time, N_0 is the desired number of particles in the buffer, and N is their current number in the buffer. If $\Delta N > 0$, new particles are inserted into the buffer using the USHER[53] algorithm. The latter performs energy minimization until either an energetically acceptable position for the particle insertion is found or the maximum number of iterations is reached. When simulating complex molecules, e.g., star polymers,[54] AdResS is used to facilitate their insertion.

In addition, the buffers are utilized for the imposition of the boundary conditions, which are applied with external forces $\mathbf{f}_i$ that act only on the particles in the buffers. The forces are determined by the momentum balance at the open boundary, using[37,40]

$$\mathbf{J}A \cdot \hat{\mathbf{n}} = \sum_{i \in B} \mathbf{f}_i + \sum_{i'} \frac{\Delta(m_{i'}\mathbf{v}_{i'})}{\Delta t}, \tag{21}$$

where $\mathbf{J}$ is the momentum flux tensor, A is the area of the interface between buffer and ROI, and $\hat{\mathbf{n}}$ is the unit normal vector of the boundary surface, pointing toward the center of the simulation box. The index i runs over all particles in the buffer, while i' runs over all particles inserted or deleted in the last time step. The momentum change for an inserted particle is $\Delta(m_{i'}\mathbf{v}_{i'}) = m_{i'}\mathbf{v}_{i'}$ and for a deleted particle, $\Delta(m_{i'}\mathbf{v}_{i'}) = -m_{i'}\mathbf{v}_{i'}$. Considering equilibrium boundary conditions of a constant normal load, the boundary condition reads as follows:

$$\mathbf{J}A \cdot \hat{\mathbf{n}} = p_{xx}A\hat{\mathbf{n}}, \tag{22}$$

where p_{xx} is the equilibrium pressure. Adding a term that applies equally opposite forces to the left and right buffer, expressed as

$$\mathbf{J}A \cdot \hat{\mathbf{n}} = p_{xx}A\hat{\mathbf{n}} + p_{xy}A\hat{\mathbf{t}}, \tag{23}$$

induces shear flow. Here, p_{xy} is the shear stress, and $\hat{\mathbf{t}}$ is a unit vector, i.e., $\hat{\mathbf{t}} = \hat{\mathbf{e}}_y$ at the right buffer and $\hat{\mathbf{t}} = -\hat{\mathbf{e}}_y$ at the left buffer. By introducing a sinusoidal disturbance on the left buffer with

$$\mathbf{J}A \cdot \hat{\mathbf{n}} = p_{xx}A\hat{\mathbf{n}} + \Delta p \sin(2\pi\nu t)A\hat{\mathbf{n}}, \tag{24}$$

an acoustic wave is generated, where Δp is the amplitude of the imposed pressure wave. The sinusoidal force is applied at each time step and the wave is left to propagate through the simulation box.

III. COMPUTATIONAL DETAILS

All simulations of liquid water under ambient conditions are performed using Mirheo,[45] an open-source, high-performance, GPU-accelerated code designed for simulating flows at milli- and micro-scales. Mirheo has been extended to support simulations using the OBMD method. For equilibrium and shear flow simulations, we use a simulation box (L_x, L_y, L_z) of dimensions $L_x = 30$ nm and $L_y = L_z = 10$ nm. To minimize spurious reflections of unattenuated waves at the ROI-buffer boundary, the simulation box should be sufficiently long in the propagation direction when simulating ultrasound waves so that the wave amplitude is relatively low at the edge. When exploring attenuation and phase velocity frequency dependence, we choose simulation boxes with ROI lengths equivalent to about six wavelengths. In addition, the introduction of non-reflective boundaries that absorb the incoming wave could further help reduce these reflections.[55] The buffer size is always $L_B = 0.15L_x$. The equations of motion are integrated using a modified velocity-Verlet algorithm with $\lambda = 1/2$,[21] where the time step for equilibrium and shear flow simulations is $\Delta t = 0.01$ ps for DPD and MDPD, and $\Delta t = 0.02$ ps for all simulations using the Martini 3 water model. In DPD and MDPD ultrasound simulations, one wave period is covered in 300 time steps. Equilibrium and shear flow simulations are conducted for 20 ns, with the first 1 ns used for equilibration and the rest 19 ns used for the production run. Ultrasound simulations are performed for 150 periods, where the last 100 are used for analysis. The normal load (p_{xx}) for DPD model simulations is determined from canonical ensemble simulations, while for the MDPD and Martini 3 model, we use $p_{xx} = 1$ bar.

The conversion between the simulation and physical scales is set through elementary units, the mass unit U_M, the length unit U_L, and the time unit U_T. They are determined using

$$U_M = m_0 N_m, \tag{25}$$

$$U_L = (\rho V_0 N_m)^{1/3}, \tag{26}$$

$$U_T = \sqrt{\frac{U_M U_L^2}{U_E}}, \tag{27}$$

where N_m is the mapping number, the number of water molecules represented by one computational particle, m_0 and V_0 are the mass and volume of one water molecule, respectively, ρ is the number density in simulation units, and U_E is the energy scale. For DPD and MDPD simulations, $U_E = k_B T$, while for simulations using the Martini 3 model, the energy scale is set to $U_E = 4.65$ kJ mol^{-1}.

A. Dissipative particle dynamics

This study examines two DPD mappings, i.e., $N_m = 4$ and $N_m = 8$.[56] The particle number density in both mappings is set to $\rho = 3\ U_L^{-3}$. This is a reasonable choice, as the quadratic EOS only holds for sufficiently high densities $(\rho > 2\ U_L^{-3})$.[21] The repulsive parameter a is determined based on the formulation by Groot *et al.*[21,57] as

$$a = \frac{N_m \kappa_{\exp}^{-1} - 1}{2\tilde{\alpha}\rho} \tag{28}$$

TABLE I. DPD parameters for 4-to-1 and 8-to-1 mappings.

Parameter	N_m	a	ρ	r_c	T	U_L	U_M	U_T
Unit	/	$U_M U_L/U_T^2$	U_L^{-3}	U_L	K	nm	10^{-25} kg	ps
	4	103.96	3.0	1.0	300	0.711	1.196	3.83
	8	209.6	3.0	1.0	300	0.893	2.39	6.83

(in units of U_E/U_L), where $\kappa_{\text{exp}}^{-1} \approx 16$ is the experimental dimensionless compressibility of water at 300 K.[21] For both mappings, we use the DPD thermostat with $\gamma = 4.5U_M/U_T$ and $s = 1.0$. The parameters and elementary units for DPD models are presented in Table I.

B. Many-body dissipative particle dynamics

Next, we utilize the MDPD water model. For $N_m = 3$, we use the parameters presented by Ghoufi and Malfreyt,[58] while the parameters for $N_m = 4$ and $N_m = 8$ are determined following the modified parameterization by Vanya *et al.*,[59,60] which reproduces the density, the surface tension and the compressibility of the fluid. Similar to the DPD model, the DPD thermostat with $\gamma = 4.5U_M/U_T$ and $s = 1.0$ is employed. The parameters used are presented in Table II.

C. Martini 3 water model

Finally, we employ the Martini 3 water model, which represents four heavy atoms with a single interaction site.[42,61] The cutoff of the Lennard-Jones (LJ) pair potential is set to $r_c^{LJ} = 1.1$ nm and the DPD thermostat with $\gamma = 1.0$ Da ps^{-1}, $s = 1.0$, and cutoff $r_c^{DPD} = 1.2$ nm is applied. The parameters and unit conversions for simulations of Martini 3 model are presented in Table III.

D. Analysis

To determine the equilibrium pressure for the DPD model, we perform canonical ensemble simulations and compute the pressure with the virial theorem,

$$p = \rho k_B T + \frac{1}{3V}\sum_{i<j}\langle \mathbf{F}_{ij}\cdot\mathbf{r}_{ij}\rangle. \tag{29}$$

Here, V is the volume, and the angular brackets denote ensemble averages. By varying the density of the systems and calculating the pressure using the virial theorem, we determine the EOS. The latter is also constructed using OBMD by varying the normal load imposed on the buffers and evaluating the density to which the open system relaxes. An example of the OBMD equilibrium mass density profile is in the supplementary material, Fig. S1. The speed of sound is determined using

$$c = \sqrt{\frac{\partial p}{\partial \rho_m}} \tag{30}$$

at $\rho_m = 10^3$ kg/m^3.

When applying equally opposite forces according to Eq. (23), a linear velocity profile through the ROI is established. By fitting a linear function to the computed data, the shear rate is calculated using $\dot{\gamma} = \partial v_y/\partial x$. Ultimately, the shear viscosity η is derived from shear rates at different shear stresses as

$$\eta = p_{xy}/\dot{\gamma}. \tag{31}$$

To analyze ultrasound simulations,[24] the ROI is divided into $N_x = 50$ equal bins along the x axis. The density variation through the ROI is computed every ten time steps, followed by averaging the density over multiple cycles for the same snapshot within a cycle. By fitting a sinusoidal function $\rho_i(t) = \rho_0 + \Delta\rho_i \sin(\omega t + \varphi)$, describing the density variation in the ith bin, where φ is the phase, we get the sound wave amplitude $\Delta\rho_i$ for each bin. Next, the attenuation coefficient is determined by fitting an exponentially decaying function $\Delta\rho(x) = \Delta\rho_0 \exp(-\alpha x)$ to the computed data. To determine the speed of sound, we examine the density variation across ROI in a particular snapshot of a cycle t_j. In our simulations, we remain within the linear acoustic regime and consider the solution to Eq. (3). For larger density amplitudes, the Burgers' equation should be applied to describe the acoustic wave.[32,33,47] The speed of sound is obtained from the wavenumber k as $v_p = \omega/k$, where k is determined by fitting a damped traveling wave function to the calculated data using

$$\rho_j(x) = \rho_0 + \Delta\rho_0 \sin(\omega t_j - kx + \varphi)\exp(-\alpha x). \tag{32}$$

The bulk viscosity was calculated from simulations of the canonical ensemble. We use the generalized Green–Kubo equations,[62–64]

$$\eta_B = \frac{V}{k_B T}\int_0^\infty \mathrm{d}t\left\langle I^C(0)I^C(t) + I^D(0)I^D(t)\right\rangle, \tag{33}$$

TABLE III. Martini 3 parameters.

Parameter	N_m	r_c^{LJ}	ϵ	σ	r_c^{DPD}	γ	U_L	U_M	U_T	U_E
Unit	/	nm	U_E	U_L	nm	Da/ps	nm	10^{-25} kg	ps	kJ/mol
	4	1.1	1.0	1.0	1.2	4.5	0.47	1.196	1.85	4.65

TABLE II. MDPD parameters for 3-to-1, 4-to-1, and 8-to-1 mappings.

Parameter	N_m	a	b	ρ	r_c	r_d	T	U_L	U_M	U_T
Unit	/	$U_M U_L/U_T^2$	$U_M U_L/U_T^2$	U_L^{-3}	U_L	U_L	K	nm	10^{-25} kg	ps
	3	−50.0	25.0	6.88	1.0	0.75	298	0.853	0.896	3.98
	4	−26.0	12.1	11.28	1.0	0.65	300	1.106	1.1952	5.943
	8	−43.2	27.6	10.09	1.0	0.65	300	1.343	2.3904	10.205

where $I^C(t)$ and $I^D(t)$ are the kinetic and dissipative projected momentum current, respectively,

$$I^C(t) = \frac{1}{3}\sum_k \left[\sigma^C_{kk}(t) - \langle\sigma^C_{kk}\rangle\right], \tag{34}$$

$$I^D(t) = \frac{1}{3}\sum_k \left[\sigma^D_{kk}(t) - \langle\sigma^D_{kk}\rangle\right], \tag{35}$$

and the stress tensor is calculated using the Irving–Kirkwood formula,[65]

$$\sigma^C_{kl} = \frac{1}{V}\sum_{i<j} r_{ijk}(t)F^C_{ijl} + \frac{1}{V}\sum_i mv_{ik}(t)v_{il}(t),$$
$$\sigma^D_{kl} = \frac{1}{V}\sum_{i<j} r_{ijk}(t)F^D_{ijl}(t). \tag{36}$$

The convergence of bulk viscosity from Eq. (33) is shown in Fig. S3 in the supplementary material.

IV. RESULTS AND DISCUSSION

We first investigate the thermodynamic behavior of the DPD water model, given by the EOS. Following the analytical framework described in Sec. III D, Fig. 2 compares the EOS obtained from simulations performed in the canonical ensemble and using the OBMD. As depicted, the computed data are in good agreement with each other and with the quadratic EOS, which for the DPD model reads as

$$p = \rho k_B T + \tilde{\alpha} r_c^4 a \rho^2. \tag{37}$$

In Table IV, we present the properties of the different water models used, calculated with OBMD, and compare them to experimentally determined values. The EOS is determined only for the DPD models with 4-to-1 and 8-to-1 mappings, with the speed of sound calculated from the fitted quadratic function. For MDPD and Martini 3, the speed of sound at water density is determined from Eq. (30) using the central difference method. The MDPD EOS is highly sensitive to density variations in negative pressure regions, which OBMD simulations could not resolve due to phase separation.[66] Similarly, the Martini 3 water model produced only slight equilibrium density variations within the simulated pressure range, which is reflected in the high speed of sound. Further increases in external pressure are limited by the hard-core nature of the potential. Another potential method to infer the EOS of Martini 3 water might involve calculating the low-frequency phase velocity from ultrasound simulations at different system densities. However, this approach is challenging, as the density tends to approach that of real water, regardless of the initial density set.

TABLE IV. Speed of sound c and viscosity η of the different water models computed using OBMD.

Model	c (m/s)	η (mPa s)
DPD 4-to-1	1498 ± 2	0.0948 ± 0.0003
DPD 8-to-1	1511 ± 2	0.210 ± 0.001
MDPD 3-to-1	1715.6 ± 0.1	0.4503 ± 0.0006
MDPD 4-to-1	1260.4 ± 0.1	0.1349 ± 0.0004
MDPD 8-to-1	1232.6 ± 0.1	0.1881 ± 0.0008
Martini 3	4039 ± 1	0.57 ± 0.01
References	1479[69]	0.890[69]

Table IV shows that while DPD reproduces the speed of sound in water, it does not simultaneously reproduce its viscosity. Similarly, other supramolecular water models yield lower viscosity compared to the experimentally determined one, with the Martini 3 model exhibiting the closest value. To this end, the viscosity could be increased by incorporating an additional thermostat, i.e., the transverse dissipative particle dynamics (TDPD) thermostat,[67,68] which offers a more sensitive and precise means of controlling the viscosity than the standard DPD thermostat.

We proceed by imposing acoustic waves of different frequencies, where the amplitude of the imposed ultrasound wave in DPD simulations is set to $\Delta p = 0.5 p_{xx}$, while the amplitude is set to 600 and 1000 bar for MDPD and Martini 3 systems, respectively, to obtain a discernible density variation signal $\Delta\rho_0/\rho_0 > 0.02$. For all models, the cycle-averaged density variation is consistent with the solution of the traveling wave equation. As an example, Fig. 3 shows the

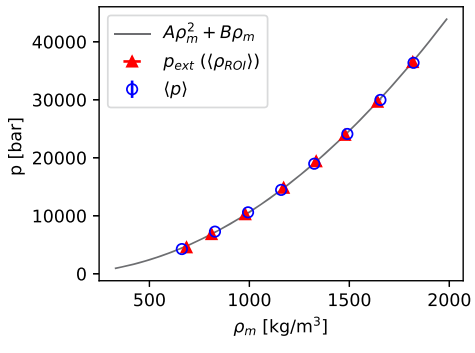

FIG. 2. EOS computed by performing closed (hollow blue circles) and OBMD (full red triangles) simulations with the DPD 4-to-1 model. The speed of sound is determined by fitting the quadratic EOS of the DPD model, represented by the black line. The standard error is smaller than the marker size.

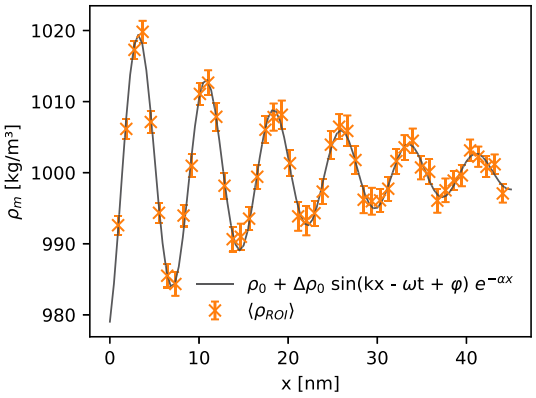

FIG. 3. Computed density variation through the ROI using the DPD 4-to-1 model for an ultrasound wave of frequency $\nu = 0.2$ THz. The error bars represent the associated standard error, and the black line corresponds to the analytical solution.

TABLE V. Phase velocity v_p and ultrasound attenuation α at 0.13 and 0.27 THz for different supramolecular water models calculated using OBMD.

Model	v_p (0.13 THz) (m/s)	α (0.13 THz) (1/μm)	v_p (0.27 THz) (m/s)	α (0.27 THz) (1/μm)
DPD 4-to-1	1502 ± 2	25 ± 1	1528 ± 8	80 ± 2
DPD 8-to-1	1612 ± 37	41 ± 2	1620 ± 14	93 ± 1
MDPD 3-to-1	1723 ± 18	36 ± 3	1871 ± 42	116 ± 9
MDPD 4-to-1	1330 ± 21	46 ± 8	1476 ± 46	149 ± 12
MDPD 8-to-1	1306 ± 31	58 ± 5	1312 ± 78	142 ± 10
Martini 3	1525 ± 19	85 ± 1	1433 ± 75	151 ± 1

cycle-averaged mass density variation through the ROI for the DPD 4-to-1 model. Similar figures for all models used are shown in Fig. S2 of the supplementary material.

The computed phase velocities v_p and attenuation coefficients α are presented in Table V. For all supramolecular water models, the phase velocities are of the expected order of magnitude, and, as anticipated, waves with higher frequency exhibit greater attenuation. The phase velocity increases with frequency for all models except for Martini 3, which, contrary to the result presented in Table IV, closely reproduces the experimental speed of sound in water. Nevertheless, we found that the results for the Martini 3 model were the most unstable among the models studied, showing sensitivity to the averaging process. Consequently, the Martini 3 model appears to be less suitable for acoustic wave simulations within the OBMD framework compared to DPD and MDPD.

Next, we investigate in more detail the influence of DPD cutoff and thermostat parameters on the viscosity, speed of sound, and attenuation. We choose the DPD 4-to-1 model, as presented in Table I, as a representative water model. Subsequently, each of the three parameters r_c, γ, and s are varied individually, while keeping the others constant. By modifying γ, we influence the ratio between the stochastic and the conservative forces. In contrast, changing the cutoff r_c alters the interaction range, which is equivalent to a change in the effective density of the system.[70] The complete collection of parameters used in this study is presented in Table VI.

In the limit of small conservative parameters, i.e., when $ar_c/k_BT \ll 1$, the DPD viscosity consists of two contributions, a kinetic diffusive part η_K and a dissipative part η_D, so that $\eta = \eta_K + \eta_D$.[21,71] In this limit, the radial distribution function is constant, $g(r) = 1$. The kinetic part is attributed to the momentum exchange between the diffusive particles and is in the limit $a \to 0$ proportional to the self-diffusion coefficient of the fluid. In contrast, the dissipative part stems from the dissipative forces that reduce the relative velocities of the particle pairs. It can be evaluated theoretically by considering shear stress in a DPD fluid under uniform shear flow. For the general case of $r_c > 0$ and $0 < s \leq 1$, the contributions are

TABLE VI. Parameters used in the DPD parameter study.

r_c (U_L)	0.8, 0.9, 1.0
γ (U_M/U_T)	2.5, 3.5, 4.5, 5.5, 6.5
s (/)	0, 0.25, 0.5, 0.75, 1.0, 2.0

$$\eta_D = \frac{4\pi\gamma r_c^5 \rho^2}{5(s+1)(s+2)(2s+1)(2s+3)(2s+5)}, \tag{38}$$

$$\eta_K = \frac{3(2s+1)(2s+2)(2s+3)mk_BT}{16\pi r_c^3 \gamma}. \tag{39}$$

In addition, potential interactions contribute to the viscosity. The potential term becomes particularly relevant when increasing the repulsion parameter $(ar_c/k_BT \gg 1)$.[72] It has been shown that while the kinetic viscosity decreases with increasing a, the dissipative contribution remains nearly independent of it. Here, we address the regime of high conservative forces, where the viscosity is determined by a combination of dissipative and potential terms.[72] We summarize the main results of the DPD parameter study in Fig. 4.

As shown in Fig. 4 (upper panels), shear viscosity increases linearly with increasing dissipative force parameter γ and decreases with increasing parameter s. Comparing this observation with the theoretical predictions of Eqs. (38) and (39), we confirm that the dissipative term governs over the kinetic contribution in the large repulsion regime.[72] Moreover, the attenuation coefficient follows a similar trend, increasing with γ and decreasing with s (middle panels of Fig. 4), as observed for the shear viscosity, confirming the linear relationship between attenuation and viscosity proposed by the thermoviscous attenuation theory, see Eq. (10). Notably, the attenuation

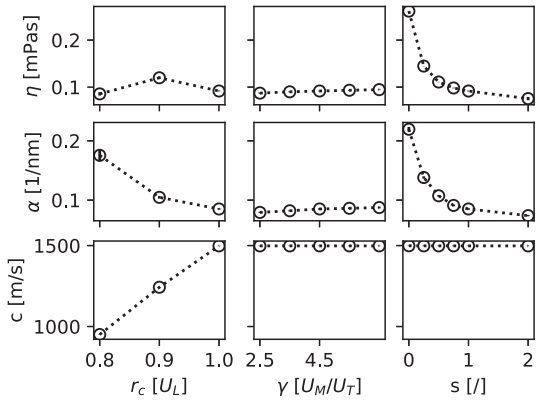

FIG. 4. Calculated viscosity η, attenuation coefficient α at 0.27 THz, and speed of sound c as a function of parameters r_c, γ, and s. The standard error is smaller than the marker size.

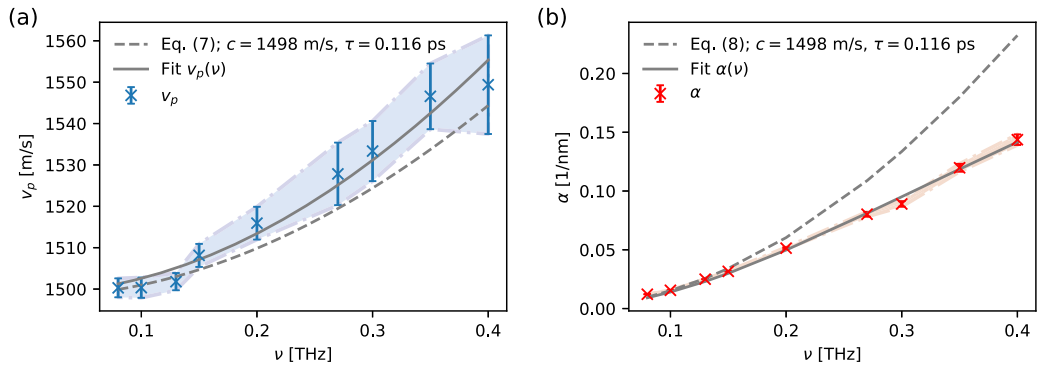

FIG. 5. Computed phase velocity v_p (a) and attenuation coefficient α (b) as functions of frequency ν for the DPD 4-to-1 mapping, where the shaded area indicates the standard error of the data points. In panel (a), the gray solid line represents the theoretical fit of Eq. (7), with $\tau_s = (0.128 \pm 0.004)$ ps and $c = (1498 \pm 2)$ m/s. In panel (b), the gray solid line is the fit of Eq. (8), with $\tau_s = (0.44 \pm 0.04)$ ps and $c = (5.9 \pm 0.2) \times 10^3$ m/s. The dashed lines represent the theoretical predictions from Eqs. (7) and (8) using the values computed in this work for the DPD 4-to-1 model ($\eta = 0.0948$ mPas, $\eta_B = 0.135$ mPas, and $c = 1498$ m/s).

is uncorrelated with viscosity only in the case of the changing cutoff. We observe higher attenuation when a shorter cutoff is used, as acoustic energy is rapidly dissipated due to the short-range interactions. On the other hand, the speed of sound, determined from the EOS computed using OBMD is independent of γ and s but increases significantly with r_c, as shown in Fig. 4 (lower panels). This is consistent with the theoretical prediction for the thermodynamic speed of sound,

$$c = \sqrt{\frac{k_B T}{m} + \frac{2\tilde{\alpha} a r_c^4 \rho}{m}}, \tag{40}$$

derived from the DPD EOS, Eq. (37).

Finally, we investigate the influence of wave frequency on phase velocity v_p and attenuation coefficient α using the DPD 4-to-1 model. Theoretical predictions from Eqs. (7) and (8) using the properties computed in this work (dashed lines shown in Fig. 5) show excellent agreement with our simulation results, particularly for the phase velocity [Fig. 5(a)], where the fitted values closely match the computed values. However, the data points and theoretical predictions for the attenuation coefficient diverge in the high-frequency limit [Fig. 5(b)], which may indicate that simulations underestimate the attenuation in this regime.

It should be noted that in our simulations, the attenuation is significantly lower than in experiments, which is a consequence of the low viscosity of our DPD fluid. From our simulations, we find $\tau_s \approx 0.116$ ps. This is about an order of magnitude lower than the real value $\tau_s \approx 1.6$ ps, Eq. (4), consistent with the lower viscosity of the DPD fluid compared to water.

V. CONCLUSIONS

In this work, we studied acoustic properties, i.e., speed of sound, and ultrasound attenuation, of liquid water employing different supramolecular models. The comparison provides information on the strengths and limitations of each water model in terms of its ability to simulate realistic water behavior under non-equilibrium conditions. Notably, all models, i.e., DPD, MDPD, and Martini 3, successfully reproduce the density signal associated with a traveling wave in response to a sinusoidal pressure disturbance, despite the significantly higher pressure required to generate a detectable density signal in the Martini 3 and MDPD models. In addition, the observed phase velocities are of the expected order of magnitude, further validating the efficacy of these models in simulating acoustic phenomena. Our simulation results agree with the predictions of thermoviscous attenuation, accurately reproducing both the dispersion and the frequency-dependence of attenuation in the fluid.

The presented method is a significant first step toward developing a more general virtual ultrasound machine. This approach allows us to directly examine the excitation modes of biomolecules in water and quantify their presence within the simulation box.[5] The ultimate aim is to extend this method to simulate ultrasonic waves at a larger scale, specifically targeting lower frequencies in the MHz range, where the challenge is overcoming freezing artifacts that arise when moving beyond the molecular scale. Moreover, our methodology holds potential for a wide range of applications beyond biomolecular studies. Refining the simulation parameters and models allows us to explore complex fluid dynamics scenarios, including multiphase flows and interactions in heterogeneous systems. The ability to simulate ultrasound propagation in such a detailed manner opens up new possibilities for research in soft matter physics, materials science, and biomedical engineering.

SUPPLEMENTARY MATERIAL

The supplementary material includes the equilibrium OBMD mass density profile, cycle-averaged density signals corresponding to ultrasound waves at various frequencies for all models, and the convergence of the bulk viscosity calculation.

ACKNOWLEDGMENTS

The authors acknowledge the financial support under ERC Advanced Grant (Grant No. 885155) from the European Research Council. The authors also acknowledge the financial support

from the Slovenian Research and Innovation Agency (Grant No. P1-0002). Finally, the authors acknowledge the HPC RIVR consortium (www.hpc-rivr.si) and EuroHPC JU (eurohpc-ju.europa.eu) for providing computing resources of the HPC system Vega at the Institute of Information Science (www.izum.si).

AUTHOR DECLARATIONS

Conflict of Interest

The authors have no conflicts to disclose.

Author Contributions

Maša Lah: Conceptualization (equal); Methodology (equal); Software (equal); Validation (equal); Visualization (equal); Writing – original draft (lead); Writing – review & editing (equal). **Nikolaos Ntarakas**: Conceptualization (equal); Methodology (equal); Software (equal); Validation (equal); Visualization (equal); Writing – original draft (supporting); Writing – review & editing (equal). **Tilen Potisk**: Conceptualization (equal); Methodology (equal); Software (equal); Supervision (equal); Validation (equal); Writing – original draft (supporting); Writing – review & editing (equal). **Petra Papež**: Conceptualization (equal); Methodology (equal); Software (equal); Supervision (equal); Validation (equal); Visualization (equal); Writing – original draft (equal); Writing – review & editing (equal). **Matej Praprotnik**: Conceptualization (lead); Funding acquisition (lead); Methodology (lead); Resources (lead); Software (equal); Supervision (lead); Validation (equal); Writing – original draft (equal); Writing – review & editing (equal).

DATA AVAILABILITY

The data that support the findings of this study are available from the corresponding author upon reasonable request.

REFERENCES

[1]T. G. Leighton, "What is ultrasound?," Prog. Biophys. Mol. Biol. **93**, 3 (2007).
[2]J. Sundaram, B. R. Mellein, and S. Mitragotri, "An experimental and theoretical analysis of ultrasound-induced permeabilization of cell membranes," Biophys. J. **84**, 3087 (2003).
[3]E. Chatani, Y.-H. Lee, H. Yagi, Y. Yoshimura, H. Naiki, and Y. Goto, "Ultrasonication-dependent production and breakdown lead to minimum-sized amyloid fibrils," Proc. Natl. Acad. Sci. U. S. A. **106**, 11119 (2009).
[4]S. Yamazaki, M. Harata, T. Idehara, K. Konagaya, G. Yokoyama, H. Hoshina, and Y. Ogawa, "Actin polymerization is activated by terahertz irradiation," Sci. Rep. **8**, 9990 (2018).
[5]P. Papež, F. Merzel, and M. Praprotnik, "Sub-THz acoustic excitation of protein motion," J. Chem. Phys. **159**, 135101 (2023).
[6]U. Adhikari, A. Goliaei, and M. L. Berkowitz, "Mechanism of membrane poration by shock wave induced nanobubble collapse: A molecular dynamics study," J. Phys. Chem. B **119**, 6225 (2015).
[7]V. H. Man, M. S. Li, P. Derreumaux, J. Wang, T. T. Nguyen, S. Nangia, and P. H. Nguyen, "Molecular mechanism of ultrasound interaction with a blood brain barrier model," J. Chem. Phys. **153**, 045104 (2020).
[8]B. Krasovitski, V. Frenkel, S. Shoham, and E. Kimmel, "Intramembrane cavitation as a unifying mechanism for ultrasound-induced bioeffects," Proc. Natl. Acad. Sci. U. S. A. **108**, 3258 (2011).
[9]M. O. Steinhauser and T. Schindler, "Particle-based simulations of bilayer membranes: Self-assembly, structural analysis, and shock-wave damage," Comput. Part. Mech. **4**, 69 (2017).
[10]H. Okumura and S. G. Itoh, "Amyloid fibril disruption by ultrasonic cavitation: Nonequilibrium molecular dynamics simulations," J. Am. Chem. Soc. **136**, 10549 (2014).
[11]M. Hoang Viet, P. Derreumaux, and P. H. Nguyen, "Nonequilibrium all-atom molecular dynamics simulation of the bubble cavitation and application to dissociate amyloid fibrils," J. Chem. Phys. **145**, 174113 (2016).
[12]Y. Sliozberg and T. Chantawansri, "Damage in spherical cellular membrane generated by the shock waves: Coarse-grained molecular dynamics simulation of lipid vesicle," J. Chem. Phys. **141**, 184904 (2014).
[13]L. E. Kinsler, A. R. Frey, A. B. Coppens, and J. V. Sanders, *Fundamentals of Acoustics* (Wiley, New York, 2000).
[14]A. D. Pierce, *Acoustics: An Introduction to its Physical Principles and Applications* (Springer, Cham, 2019).
[15]D. Trevena, "Ultrasonic waves in liquids," Contemp. Phys. **10**, 601 (1969).
[16]P. K. Kythe, *An Introduction to Boundary Element Methods* (CRC Press, Boca Raton, 2020).
[17]F. Ihlenburg, *Finite Element Analysis of Acoustic Scattering* (Springer, New York, 1998).
[18]B. J. Alder and T. Wainwright, "Decay of the velocity autocorrelation function," Phys. Rev. A **1**, 18 (1970).
[19]L. D. Landau and E. M. Lifshitz, *Fluid Mechanics* (Pergamon, Oxford, 1987).
[20]J. J. Monaghan, "Smoothed particle hydrodynamics," Rep. Prog. Phys. **68**, 1703 (2005).
[21]R. D. Groot and P. B. Warren, "Dissipative particle dynamics: Bridging the gap between atomistic and mesoscopic simulation," J. Chem. Phys. **107**, 4423 (1997).
[22]P. Hoogerbrugge and J. Koelman, "Simulating microscopic hydrodynamic phenomena with dissipative particle dynamics," Europhys. Lett. **19**, 155 (1992).
[23]P. Español and P. Warren, "Statistical mechanics of dissipative particle dynamics," Europhys. Lett. **30**, 191 (1995).
[24]P. Papež and M. Praprotnik, "Dissipative particle dynamics simulation of ultrasound propagation through liquid water," J. Chem. Theory Comput. **18**, 1227 (2022).
[25]Y. O. Zhang, T. Zhang, H. Ouyang, and T. Y. Li, "SPH simulation of acoustic waves: Effects of frequency, sound pressure, and particle spacing," Math. Probl. Eng. **2015**, 348314.
[26]I. Korotkin, S. Karabasov, D. Nerukh, A. Markesteijn, A. Scukins, V. Farafonov, and E. Pavlov, "A hybrid molecular dynamics/fluctuating hydrodynamics method for modelling liquids at multiple scales in space and time," J. Chem. Phys. **143**, 014110 (2015).
[27]L. Delle Site and M. Praprotnik, "Molecular systems with open boundaries: Theory and simulation," Phys. Rep. **693**, 1 (2017).
[28]G. De Fabritiis, R. Delgado-Buscalioni, and P. Coveney, "Multiscale modeling of liquids with molecular specificity," Phys. Rev. Lett. **97**, 134501 (2006).
[29]R. Delgado-Buscalioni and G. De Fabritiis, "Embedding molecular dynamics within fluctuating hydrodynamics in multiscale simulations of liquids," Phys. Rev. E **76**, 036709 (2007).
[30]J. Hu, I. Korotkin, and S. Karabasov, "A multi-resolution particle/fluctuating hydrodynamics model for hybrid simulations of liquids based on the two-phase flow analogy," J. Chem. Phys. **149**, 084108 (2018).
[31]I. Korotkin and S. Karabasov, "A generalised Landau–Lifshitz fluctuating hydrodynamics model for concurrent simulations of liquids at atomistic and continuum resolution," J. Chem. Phys. **149**, 244101 (2018).
[32]Y. Asano, H. Watanabe, and H. Noguchi, "Molecular dynamics simulation of soundwave propagation in a simple fluid," J. Chem. Phys. **153**, 124504 (2020).
[33]Y. Asano, H. Watanabe, and H. Noguchi, "Effects of vapor–liquid phase transitions on sound-wave propagation: A molecular dynamics study," Phys. Rev. Fluids **7**, 064302 (2022).
[34]S. Granick, "Motions and relaxations of confined liquids," Science **253**, 1374 (1991).
[35]M. Barisik and A. Beskok, "Equilibrium molecular dynamics studies on nanoscale-confined fluids," Microfluid. Nanofluid. **11**, 269 (2011).

[36]R. Delgado-Buscalioni, K. Kremer, and M. Praprotnik, "Concurrent triple-scale simulation of molecular liquids," J. Chem. Phys. **128**, 114110 (2008).
[37]R. Delgado-Buscalioni, J. Sablić, and M. Praprotnik, "Open boundary molecular dynamics," Eur. Phys. J. Spec. Top. **224**, 2331 (2015).
[38]M. Praprotnik, L. Delle Site, and K. Kremer, "Adaptive resolution molecular-dynamics simulation: Changing the degrees of freedom on the fly," J. Chem. Phys. **123**, 224106 (2005).
[39]M. Praprotnik, L. D. Site, and K. Kremer, "Multiscale simulation of soft matter: From scale bridging to adaptive resolution," Annu. Rev. Phys. Chem. **59**, 545 (2008).
[40]E. G. Flekkøy, R. Delgado-Buscalioni, and P. V. Coveney, "Flux boundary conditions in particle simulations," Phys. Rev. E **72**, 026703 (2005).
[41]R. Delgado-Buscalioni, "Tools for multiscale simulation of liquids using open molecular dynamics," in *Numerical Analysis of Multiscale Computations*, edited by B. Engquist, O. Runborg, and Y.-H. R. Tsai (Springer, Berlin, Heidelberg, 2012), pp. 145–166.
[42]P. C. Souza, R. Alessandri, J. Barnoud, S. Thallmair, I. Faustino, F. Grünewald, I. Patmanidis, H. Abdizadeh, B. M. Bruininks, T. A. Wassenaar *et al.*, "Martini 3: A general purpose force field for coarse-grained molecular dynamics," Nat. Methods **18**, 382 (2021).
[43]I. Pagonabarraga and D. Frenkel, "Dissipative particle dynamics for interacting systems," J. Chem. Phys. **115**, 5015 (2001).
[44]P. B. Warren, "Vapor-liquid coexistence in many-body dissipative particle dynamics," Phys. Rev. E **68**, 066702 (2003).
[45]D. Alexeev, L. Amoudruz, S. Litvinov, and P. Koumoutsakos, "Mirheo: High-performance mesoscale simulations for microfluidics," Comput. Phys. Commun. **254**, 107298 (2020).
[46]L. Hall, "The origin of ultrasonic absorption in water," Phys. Rev. **73**, 775 (1948).
[47]J. M. Burgers, "A mathematical model illustrating the theory of turbulence," Adv. Appl. Mech. **1**, 171 (1948).
[48]L. Amoudruz, A. Economides, and P. Koumoutsakos, "The volume of healthy red blood cells is optimal for advective oxygen transport in arterioles," Biophys. J. **123**, 1289 (2024).
[49]N. Spenley, "Scaling laws for polymers in dissipative particle dynamics," Europhys. Lett. **49**, 534 (2000).
[50]V. Pryamitsyn and V. Ganesan, "A coarse-grained explicit solvent simulation of rheology of colloidal suspensions," J. Chem. Phys. **122**, 104906 (2005).
[51]J. L. Jones, M. Lal, J. Noel Ruddock, and N. A. Spenley, "Dynamics of a drop at a liquid/solid interface in simple shear fields: A mesoscopic simulation study," Faraday Discuss. **112**, 129 (1999).
[52]S. Jamali, A. Boromand, S. Khani, J. Wagner, M. Yamanoi, and J. Maia, "Generalized mapping of multi-body dissipative particle dynamics onto fluid compressibility and the Flory-Huggins theory," J. Chem. Phys. **142**, 164902 (2015).
[53]R. Delgado-Buscalioni and P. V. Coveney, "USHER: An algorithm for particle insertion in dense fluids," J. Chem. Phys. **119**, 978 (2003).
[54]J. Sablić, M. Praprotnik, and R. Delgado-Buscalioni, "Open boundary molecular dynamics of sheared star-polymer melts," Soft Matter **12**, 2416 (2016).
[55]R. Delgado-Buscalioni and A. Dejoan, "Nonreflecting boundaries for ultrasound in fluctuating hydrodynamics of open systems," Phys. Rev. E **78**, 046708 (2008).
[56]J. Zavadlav, S. J. Marrink, and M. Praprotnik, "Adaptive resolution simulation of supramolecular water: The concurrent making, breaking, and remaking of water bundles," J. Chem. Theory Comput. **12**, 4138 (2016).
[57]R. Groot and K. Rabone, "Mesoscopic simulation of cell membrane damage, morphology change and rupture by nonionic surfactants," Biophys. J. **81**, 725 (2001).
[58]A. Ghoufi and P. Malfreyt, "Mesoscale modeling of the water liquid–vapor interface: A surface tension calculation," Phys. Rev. E **83**, 051601 (2011).
[59]P. Vanya, J. Sharman, and J. A. Elliott, "Invariance of experimental observables with respect to coarse-graining in standard and many-body dissipative particle dynamics," J. Chem. Phys. **150**, 064101 (2019).
[60]P. Vanya, P. Crout, J. Sharman, and J. A. Elliott, "Liquid-phase parametrization and solidification in many-body dissipative particle dynamics," Phys. Rev. E **98**, 033310 (2018).
[61]J. Zavadlav, M. N. Melo, A. V. Cunha, A. H. de Vries, S. J. Marrink, and M. Praprotnik, "Adaptive resolution simulation of MARTINI solvents," J. Chem. Theory Comput. **10**, 2591 (2014).
[62]G. Jung and F. Schmid, "Computing bulk and shear viscosities from simulations of fluids with dissipative and stochastic interactions," J. Chem. Phys. **144**, 204104 (2016).
[63]D. C. Malaspina, M. Lísal, J. P. Larentzos, J. K. Brennan, A. D. Mackie, and J. B. Avalos, "Transport coefficients from Einstein–Helfand relations using standard and energy-conserving dissipative particle dynamics methods," Phys. Chem. Chem. Phys. **25**, 12025 (2023).
[64]D. C. Malaspina, M. Lísal, J. P. Larentzos, J. K. Brennan, A. D. Mackie, and J. B. Avalos, "Green–Kubo expressions for transport coefficients from dissipative particle dynamics simulations revisited," Phys. Chem. Chem. Phys. **26**, 1328 (2024).
[65]J. Irving and J. G. Kirkwood, "The statistical mechanical theory of transport processes. IV. The equations of hydrodynamics," J. Chem. Phys. **18**, 817 (1950).
[66]R. L. Hendrikse, C. Amador, and M. R. Wilson, "A many-body dissipative particle dynamics parametrisation scheme to study behaviour at air–water interfaces," Soft Matter **19**, 3590 (2023).
[67]C. Junghans, M. Praprotnik, and K. Kremer, "Transport properties controlled by a thermostat: An extended dissipative particle dynamics thermostat," Soft Matter **4**, 156 (2008).
[68]A. Eriksson, M. Jacobi, J. Nyström, and K. Tunstrøm, "Effective thermostat induced by coarse graining of simple point charge water," J. Chem. Phys. **129**, 024106 (2008).
[69]W. Haynes, *CRC Handbook of Chemistry and Physics* (CRC Press, Boca Raton, 2014).
[70]R. M. Füchslin, H. Fellermann, A. Eriksson, and H. J. Ziock, "Coarse graining and scaling in dissipative particle dynamics," J. Chem. Phys. **130**, 214102 (2009).
[71]C. A. Marsh, G. Backx, and M. H. Ernst, "Static and dynamic properties of dissipative particle dynamics," Phys. Rev. E **56**, 1676 (1997).
[72]H. Noguchi and G. Gompper, "Transport coefficients of dissipative particle dynamics with finite time step," Europhys. Lett. **79**, 36002 (2007).